INORGANIC CHEMISTRY
FRONTIERS

RESEARCH ARTICLE

View Article Online
View Journal | View Issue

Check for updates

Cite this: *Inorg. Chem. Front.*, 2025, **12**, 8008

A low-valent alkali metal doping strategy for enhanced performance of high-entropy oxide catalysts in reverse water–gas shift reactions

Ke Wang, [a,b] Rui Zhang, [a,b] Li Liu, [a,b] Xueting Wu, [a,b] Jing Xu, *[a] Shuyan Song, *[a,b] Hongjie Zhang [a,b,c] and Xiao Wang *[a,b]

Received 8th May 2025,
Accepted 9th August 2025

DOI: 10.1039/d5qi01099c

rsc.li/frontiers-inorganic

The reverse water–gas shift (RWGS) reaction is a key pathway for catalytic CO_2 valorization. Emerging high-entropy oxide (HEO) systems exhibit great catalytic potential; however, their activity remains suboptimal. In this work, we developed a Li-doping strategy to modify the $(Mg_1Co_1Ni_1Cu_1Zn_1)O_\alpha$ (J14) high-entropy oxide (HEO) catalyst, yielding enhanced RWGS catalytic performance. The Li-doped catalyst exhibited a CO generation rate of 210 $\mu mol_{CO}\ g_{cat}^{-1}\ s^{-1}$ at 400 °C, 1.46 times higher than that of J14, with enhanced stability. Systematic characterization and experiments demonstrated that this approach effectively coordinates metal exsolution and dispersion while tailoring surface alkalinity, thereby enhancing both H_2 dissociation and CO_2 activation. Furthermore, a mechanistic shift from the redox pathway to the carbonate-associative pathway was observed. This low-valent alkali metal doping strategy offers a generalizable design principle for HEO catalysts.

Introduction

The rapid advancement of industrialization and economic growth has increased atmospheric CO_2 to unprecedented levels, causing significant environmental challenges.[1,2] Among potential solutions, catalytic conversion of CO_2 emerges as a particularly promising solution, offering the dual benefit of facilitating carbon cycle management while generating valuable chemical products.[3–8] Within this field, the reverse water–gas shift (RWGS) reaction plays a crucial role in CO_2 hydrogenation processes and serves as a fundamental step in Fischer–Tropsch synthesis.[9–11]

High-entropy oxides (HEOs), an emerging class of catalytic materials, demonstrate unique advantages including tailorable elemental configurations and lattice distortion-induced oxygen vacancy enrichment originating from their multi-component disordered structures.[12,13] Beyond conventional oxidation catalysis, recent advancements demonstrate the exceptional catalytic performance of HEOs in hydrogenation reactions.[14–17] Notably, these materials can function as self-sufficient exsolution hosts, without external metal loading, while exhibiting excellent RWGS activity.[18–20] However, their catalytic efficacy still lags behind that of well-established Pt-, Cu-, and Mo-based systems, necessitating the development of targeted HEO modification protocols to unlock their full potential.[21–25]

A key approach for enhancing the RWGS activity of a catalyst is doping with alkali metals (*e.g.*, Li, Na, K), which as evidenced by numerous studies can effectively boost catalyst basicity and consequently improve CO_2 adsorption capacity.[26–28] Additionally, within exsolution frameworks, the incorporation of low-valent cations was shown to facilitate the exsolution of metal sites.[29,30] This is attributed to the fact that low-valent cations induce lattice distortions, weakening host cation–oxygen bonds, and promote the generation of oxygen vacancies through charge compensation mechanisms, both of which enhance ion migration to drive the exsolution.[30–33] The resulting higher surface concentration of metal sites improves hydrogen accessibility, thereby enhancing overall hydrogenation activity, which is another key factor contributing to the catalytic RWGS reaction.[34–36] Therefore, a finely-controlled alkali metal doping strategy is promising for optimizing both CO_2 adsorption and H_2 activation, consequently boosting the catalytic performance.

In this work, we report enhanced RWGS performance through the strategic incorporation of low-valent alkali metals in HEO catalysts. This optimization achieved simultaneous improvement in catalytic activity and stability with limited CH_4 byproduct formation. Systematic characterization and structure–activity relationship studies revealed that moderate

[a]*State Key Laboratory of Rare Earth Resource Utilization, Changchun Institute of Applied Chemistry, Chinese Academy of Sciences, Changchun 130022, China. E-mail: songsy@ciac.ac.cn, wangxiao@ciac.ac.cn*
[b]*School of Applied Chemistry and Engineering, University of Science and Technology of China, Hefei 230026, China*
[c]*Department of Chemistry, Tsinghua University, Beijing 100084, China*

Open Access Article. Published on 02 Fuulbana 2025. Downloaded on 04/12/2025 4:41:09 AM.
This article is licensed under a Creative Commons Attribution-NonCommercial 3.0 Unported Licence.

This journal is © the Partner Organisations 2025

Open Access Article. Published on 02 Fuulbana 2025. Downloaded on 04/12/2025 4:41:09 AM.
This article is licensed under a Creative Commons Attribution-NonCommercial 3.0 Unported Licence.

Li doping promoted metallic exsolution while tuning metallic composition and dispersion, thereby facilitating H_2 adsorption and dissociation. Concurrently, Li incorporation augmented oxygen vacancy formation, stabilized adsorbed oxygen species, and enhanced moderate-strength basic sites, which collectively promoted CO_2 adsorption and activation. Mechanistic investigations identify suppressed redox pathways with enhanced associative routes and rationalize the observed methane formation.

Experimental

Experimental details can be found in the SI.

Results

Screening of alkali metal ions for doping

Spray pyrolysis was used to synthesize the $(Mg_1Co_1Ni_1Cu_1Zn_1)O_\alpha$ (named J14) high-entropy oxide (Fig. S1). Given the average +2 oxidation state of Mg, Co, Ni, Cu, and Zn in J14, monovalent cations (Li^+, Na^+, K^+) were selected for low-valent substitution. During synthesis, equimolar quantities of these ions, relative to individual metals in J14, were incorporated to prepare modified samples (named J14+Li, J14+Na, J14+K). X-ray diffraction (XRD) analysis of J14 reveals distinct peaks at 37°, 42.9°, 62.1°, 74.5°, and 78.3°, corresponding to the (111), (200), (220), (311), and (222) crystal planes of a rock salt phase structure (Fig. S2). With the introduction of Li^+, the diffraction peaks of the rock salt phase shifted to higher angles, and prominent impurity peaks at 31.8°, 34.4°, and 36.3° were assigned to the (100), (002), and (101) planes of wurtzite-type ZnO (Fig. S2). This indicates successful incorporation of Li^+ ions into the lattice, which induced segregation of Zn species from the J14 matrix. Therefore, we infer that the partial replacement of the Zn component by Li is promising for synthesizing samples with pure rock salt phases. In contrast, XRD patterns of J14+Na and J14+K revealed no discernible peak shifts compared to the parent structure, with weak ZnO impurity peaks (Fig. S2). Instead, distinct diffraction peaks corresponding to $NaNO_3$ and KNO_3 were observed, suggesting limited lattice incorporation of Na^+/K^+ ions into J14 and incomplete thermal decomposition during synthesis. To elucidate the origins of this differentiation, a systematic analysis of constituent elements' ionic radii and crystal radii in the rock salt phase structure (hexacoordination) was conducted, and the comparative data are shown in Fig. S3. It reveals that the ionic and crystal radii of Li^+ (76 pm and 90 pm, respectively) approximate those of the J14 component ions (69–94.5 pm and 83–88.5 pm, respectively), whereas the radii of Na^+ and K^+ (102/116 pm and 138/152 pm) exceed feasible matching thresholds.

Structural characterization of Li-doped J14 samples

Building on the alkali metal ion screening, we selected Li to incrementally replace Zn to synthesize a series of Li-doped J14 samples (denoted as J14-Li_xZn_y, where $x:y$ represents the feed ratio of Li to Zn atoms), and the accuracy of the synthesis was verified through inductively coupled plasma (ICP) analysis (Table S1). As shown in Fig. 1a, the XRD patterns exclusively exhibit the diffraction peaks of the pure rock-salt phase across all Li-doped samples, indicating that the partial substitution of Zn by Li did not disrupt the rock-salt structure. We magnified the 35°–45° region of the XRD patterns for clear resolution, covering the diffraction peaks of the (111) and (200) crystal planes of the rock salt structure located at 36.9° and 42.9°, as displayed in Fig. 1b. Compared to J14, the diffraction peaks in low-Li-doped samples (J14-Li_1Zn_9 and J14-Li_1Zn_3) exhibited minimal shift. As the Li content increased, the peaks shifted to higher angles (37.1° and 43.1° in J14-Li_1Zn_1, 37.5° and 43.5° in J14-Li), corresponding to a decrease in interplanar spacing, indicating that Li doping induces lattice contraction.[37] This phenomenon could be attributed to the formation of anion vacancies caused by charge compensation mechanisms.[38]

The morphology of the samples was characterized by scanning electron microscopy (SEM, Fig. 1c and S4). All samples displayed irregularly shaped particles with varying sizes, but their particle size distributions did not significantly differ. This is because the particle size is predominantly determined by the droplet diameter and solution concentration, which were both rigorously maintained constant across all sample preparations. Furthermore, energy-dispersive X-ray spectroscopy (EDX) line scanning experiments were conducted on 2–3 μm diameter particles from each sample to investigate the distribution of Mg, Co, Ni, Cu, and Zn elements (Li's X-ray energy is so low that it can hardly be detected by the EDX detector). As shown in Fig. 1d, all elemental line-scanning intensity profiles in J14 exhibited consistent trends, confirming homogeneous elemental distribution. As Li replaced Zn, Zn's signal intensity progressively decreased while the other elements remained uniformly distributed (Fig. 1e, f, and S5, 6). Although Li can hardly be experimentally detected, the homogeneous distribution of Mg, Co, Ni, Cu, and Zn, coupled with the single-phase structure, strongly suggests the uniform distribution of Li. These results demonstrate the high entropy structure of the Li-doped samples.[39] In addition, Li doping was found to contribute to a higher specific surface area *via* the Brunauer–Emmett–Teller (BET) method (Fig. S7 and Table S2).

The RWGS performance of the catalysts

The RWGS activity was evaluated in a fixed-bed reactor under the following conditions: reaction temperature ranging from 200 to 400 °C, weight hourly space velocity (WHSV) of 300 000 mL g_{cat}^{-1} h^{-1}, and pressure of 0.1 MPa. Li doping enhances CO_2 conversion compared to that for pristine J14 (Fig. 2a), although with a concomitant decrease in CO selectivity as Li content increased (Fig. 2b). At 400 °C, J14-Li demonstrated the highest CO_2 conversion (37.7%) but suffered from significantly compromised CO selectivity (<50%). In contrast, the J14-Li_1Zn_3 sample maintained both a relatively high CO_2

Open Access Article. Published on 02 Fuulbana 2025. Downloaded on 04/12/2025 4:41:09 AM.
This article is licensed under a Creative Commons Attribution-NonCommercial 3.0 Unported Licence.

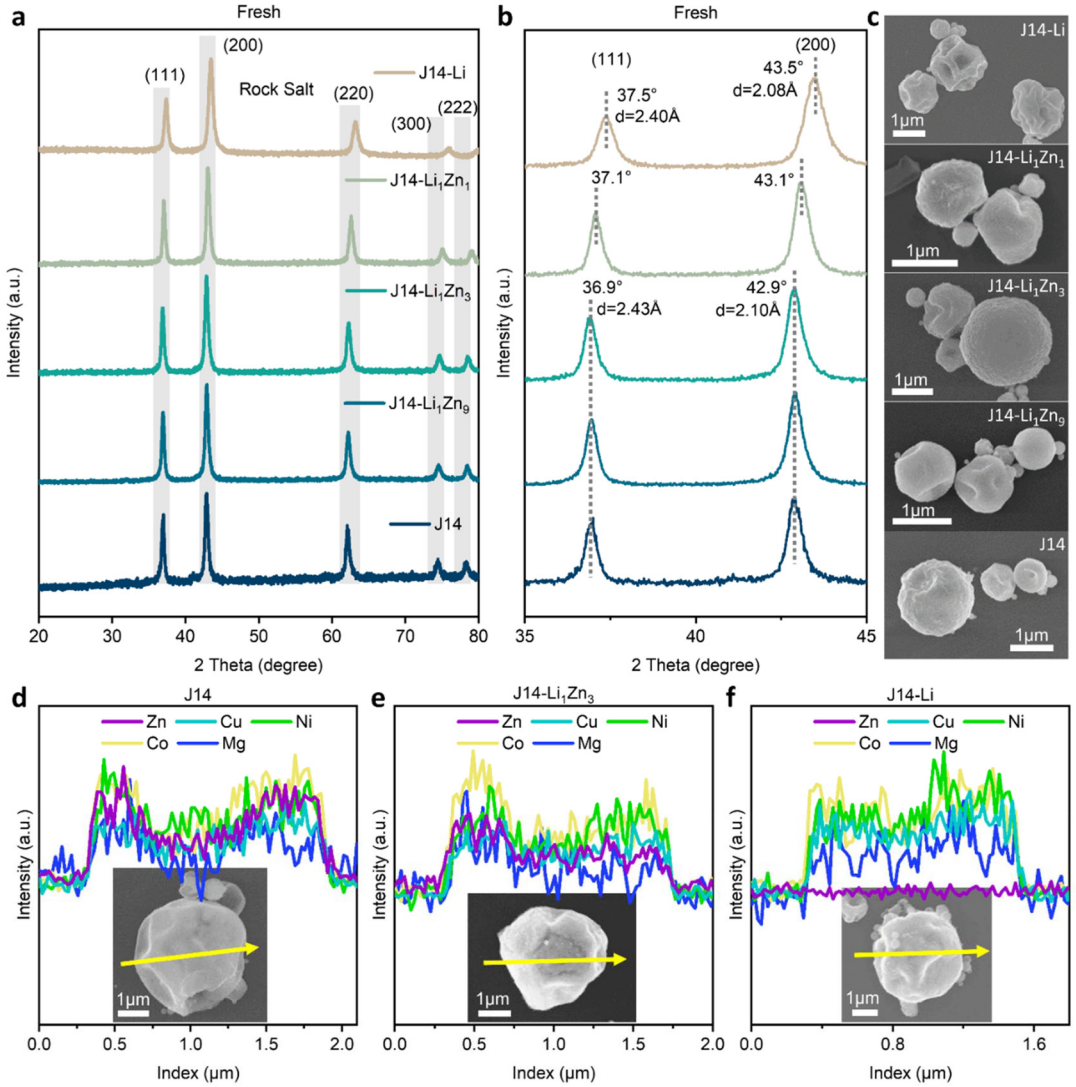

Fig. 1 Characterization of fresh samples. (a) Overall and (b) 35°–45° magnified XRD patterns, and (c) SEM images of J14-Li, J14-Li_1Zn_1, J14-Li_1Zn_3, J14-Li_1Zn_9, and J14. SEM and EDX line scanning images of J14 (d), J14-Li_1Zn_3 (e), and J14-Li (f).

conversion (26%) and excellent CO selectivity (90.4%). For better comparison, we calculated the CO formation rates for different samples (Fig. 2c). The CO yields of J14, J14-Li_1Zn_9, J14-Li_1Zn_3, J14-Li_1Zn_1, and J14-Li reached 16.1%, 21.1%, 23.5%, 20.6%, and 16.9%, respectively, exhibiting a volcano-shaped trend with J14-Li_1Zn_3 demonstrating optimal catalytic performance. Here, the CO generation rate of J14-Li_1Zn_3 reached 210 $\mu mol_{CO}\ g_{cat}^{-1}\ s^{-1}$. Based on these results, we selected J14-Li_1Zn_3 as the primary sample for subsequent studies, using the two extreme compositions (J14 and J14-Li) as references. We subsequently evaluated their stability at 400 °C, with the decay of CO_2 conversion and variation in CO selectivity over time shown in Fig. 2d and S8. After 32 h of continuous operation, J14-Li_1Zn_3 retained 70% of its initial activity, whereas J14 retained only 56% after merely 4 h, and J14-Li retained 60% after 11 h, demonstrating the superior stability of J14-Li_1Zn_3. Notably, their CO selectivity gradually increased with the prolongation of reaction time. Although J14-Li exhibited the largest increase in CO selectivity, it only reached 83.2% after 15 h of catalysis, whereas that of J14-Li_1Zn_3 reached 96.8% after 30 h. Moreover, among the state of the art non-noble and even noble metal catalysts reported recently, our J14-Li_1Zn_3 exhibits a leading rate of CO production (Table S3).

Structural evolution of the catalysts

The fresh catalyst samples inevitably undergo reconstruction under reactive atmospheres during catalytic evaluation, which critically governs their catalytic performance. BET analysis of the used catalysts showed that the Li-doped samples possessed consistently higher specific surface areas exceeding that of J14 (Fig. S9 and Table S2). However, notably, this property exhibited no strong correlation with catalytic performance, suggesting the key role of the catalyst structure. To investigate

 This journal is © the Partner Organisations 2025

Open Access Article. Published on 02 Fuulbana 2025. Downloaded on 04/12/2025 4:41:09 AM.
This article is licensed under a Creative Commons Attribution-NonCommercial 3.0 Unported Licence.

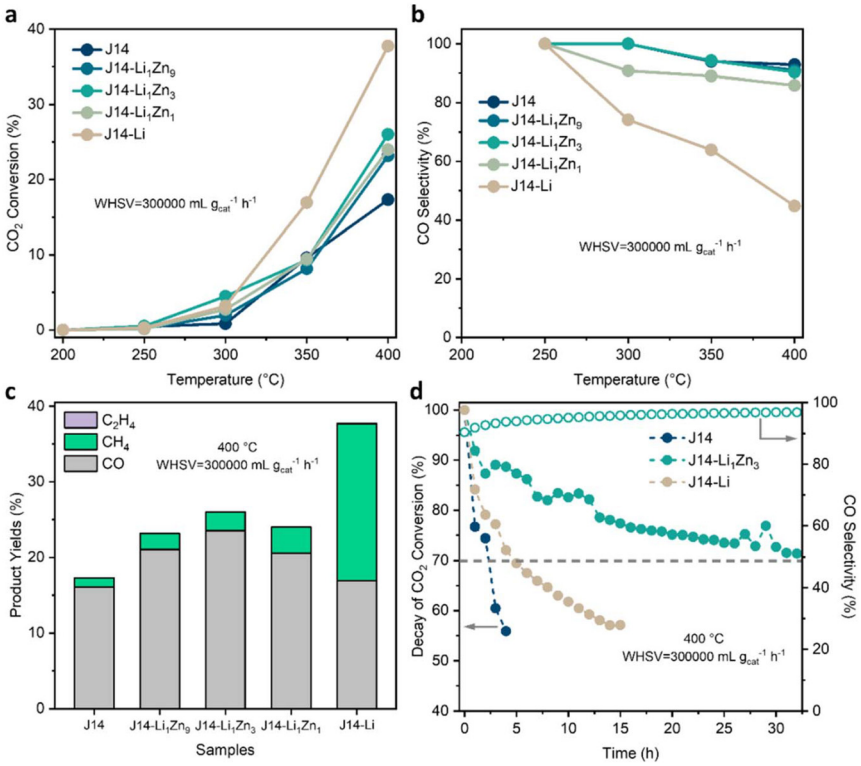

Fig. 2 RWGS performance of catalysts. The plots of CO_2 conversion (a) and CO selectivity (b) of J14, J14-Li_1Zn_9, J14-Li_1Zn_3, J14-Li_1Zn_1, and J14-Li, *versus* temperature. (c) Product distribution and yields of J14, J14-Li_1Zn_9, J14-Li_1Zn_3, J14-Li_1Zn_1, and J14-Li, at 400 °C. (d) Long-term catalytic tests of J14, J14-Li_1Zn_3, and J14-Li, at 400 °C. Reaction conditions: $CO_2/H_2/Ar$ = 24/72/4 (v/v/v); WHSV = 300 000 mL g_{cat}^{-1} h^{-1}; ordinary pressure.

the fine structures of the used catalysts, we next performed a series of characterization studies, including XRD, scanning transmission electron microscopy (STEM), and energy-dispersive X-ray spectroscopy (EDX) mapping. The XRD patterns reveal that all catalysts maintained the rock salt phase structure (Fig. 3a). Additionally, two broad peaks centered at 43°–45° and 50°–52° were observed across all samples, which could be attributed to face-centered cubic (fcc) metallic phases. These emergent features intensified progressively with the increase in Li content, suggesting an increase in metal composition. For precise peak identification, the 40°–55° region was magnified (Fig. 3b). A comparative analysis revealed that the broad peaks did not correspond to any metal element. Instead, they were located at intermediate positions between Cu and Co/Ni metal. It may be caused by overlapping of diffraction peaks of these metals or the formation of alloys. Increasing Li doping induced a shift in peak positions toward Co/Ni positions, implying an increasing Co/Ni component. Moreover, the STEM and EDX mapping images of the used J14 particles exhibit an overall uniform distribution of metal elements, apart from a handful of Co and Cu element particulate aggregates (Fig. 4a). The STEM and EDX mapping images of the used J14-Li_1Zn_3 and J14-Li show a similar picture (Fig. 4c and e). The localized magnification reveals significant aggregation of Cu and Co elements without obvious overlap (not an alloy feature),[40] while Ni, Mg, and Zn are homogeneously distributed (Fig. 4b, d and e). Among them, Cu and Co exhibit differences in the sizes of aggregates, with smaller size *versus* J14 in J14-Li_1Zn_3 and larger size in J14-Li. In conjunction with the XRD results, these results suggest that the catalysts maintain a high entropy structure after catalysis, and Cu and Co undergo exsolution without forming an alloy. Li doping could promote the metal exsolution, with moderate doping enhancing dispersivity and excessive doping triggering agglomeration.

To probe the surface states of the catalysts, we carried out X-ray photoelectron spectroscopy (XPS) analysis on the used catalysts. Cu 2p and LMM XPS analyses revealed the coexistence of Cu^{2+} and $Cu^{+/0}$ species across J14, J14-Li_1Zn_3, and J14-Li catalysts (Fig. 5a and Fig. S10).[41] The $Cu^{+/0}$ concentration increased in the order of J14 (71.6%) < J14-Li_1Zn_3 (83.6%) < J14-Li (87.7%), correlating with increasing Li incorporation. Similarly, the Co 2p spectra reveal the presence of Co^{2+} and Co^0 on the J14, J14-Li_1Zn_3, and J14-Li catalysts, with Co^0 concentrations of 6.2% for J14, 16% for J14-Li_1Zn_3, and 22.2% for J14-Li (Fig. 5b).[42] Notably, the metallic state of Ni was also identified in the Ni 2p spectra, with concentrations of 6.5%, 17.7%, and 18.5% for J14, J14-Li_1Zn_3, and J14-Li, respectively (Fig. 5c).[43] Nevertheless, no Ni aggregation was distinctly identified in the former EDX mapping findings. It suggests that Ni undergoes exsolution as well, while metallic Ni species should be present in a highly dispersed state. Meanwhile, Ni^{2+}–OH species were identified on J14-Li.[44] In addition, XPS

Open Access Article. Published on 02 Fuulbana 2025. Downloaded on 04/12/2025 4:41:09 AM.
This article is licensed under a Creative Commons Attribution-NonCommercial 3.0 Unported Licence.

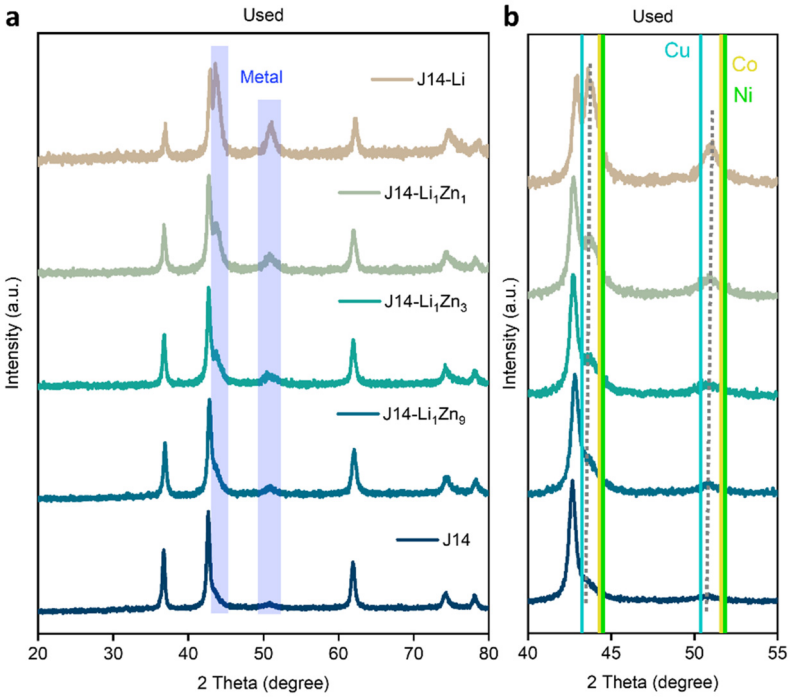

Fig. 3 (a) Overall and (b) 40°–55° magnified XRD patterns of used J14-Li, J14-Li_1Zn_1, J14-Li_1Zn_3, J14-Li_1Zn_9, and J14.

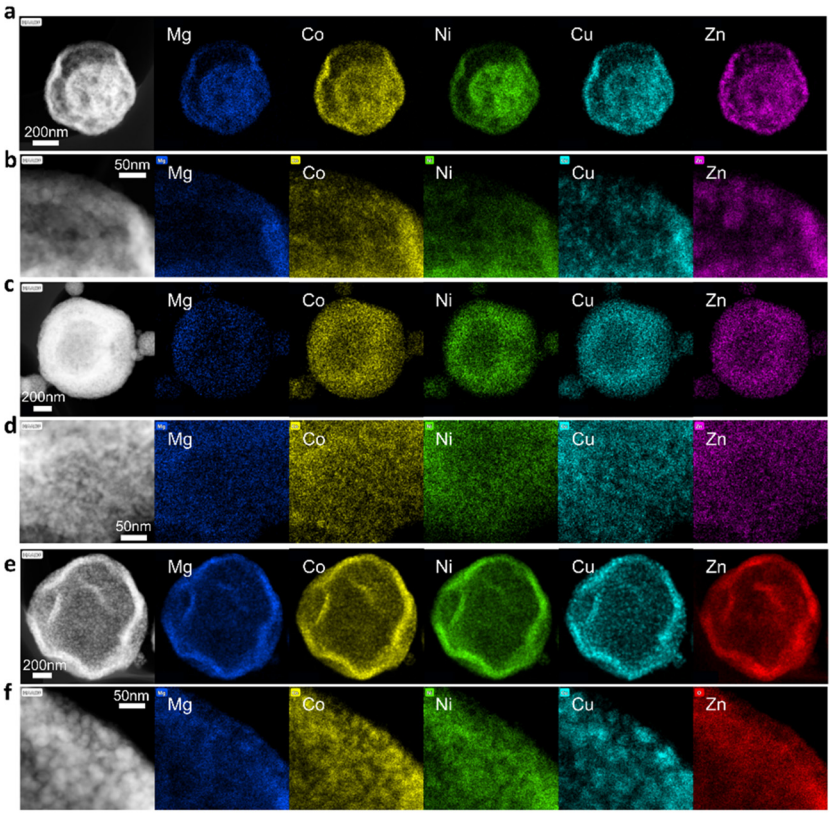

Fig. 4 Particle and localized magnified HADDF-STEM and EDX mapping images of used J14 (a and b), J14-Li_1Zn_3 (c and d), and J14-Li (e and f).

This journal is © the Partner Organisations 2025

Open Access Article. Published on 02 Fuulbana 2025. Downloaded on 04/12/2025 4:41:09 AM.
This article is licensed under a Creative Commons Attribution-NonCommercial 3.0 Unported Licence.

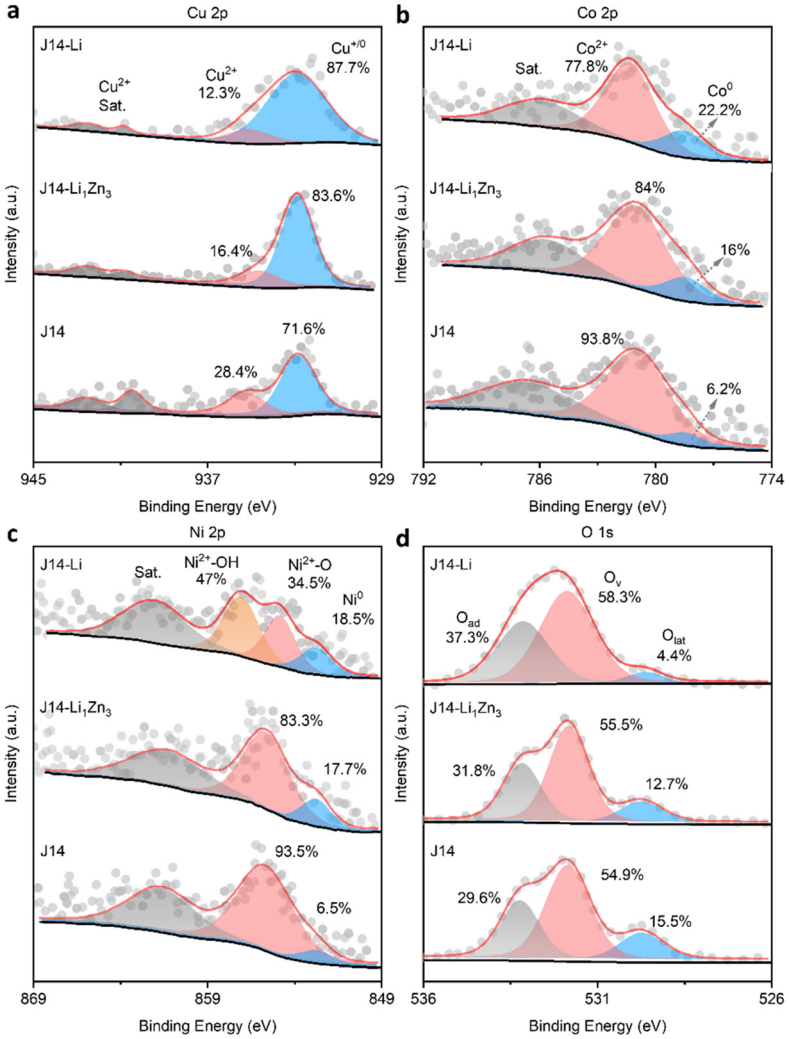

Fig. 5 XPS spectra of Cu 2p (a), Co 2p (b), Ni 2p (c), and O 1s (d) of used J14-Li, J14-Li_1Zn_3, and J14.

analysis of Mg, Zn, and Li revealed their oxidized states (Fig. S11–S13).[45–47] These results reveal that Cu dominates the metal sites, and Li incorporation promotes the exsolution of Cu, Co, and Ni metals, which is consistent with XRD results. As shown in Fig. 5d, XPS deconvolution of the O 1s spectra across all samples showed three distinct components at 529.7 eV (lattice oxygen, O_{lat}), 531.8 eV (oxygen vacancies, O_v), and 533.2 eV (adsorbed oxygen species, O_{ad}).[48] The O_{ad} primarily comprises hydroxyl groups and carbonate-related species (Fig. 5c, S11, and S13). Quantitative analysis shows that with increasing Li doping, the O_{lat} concentration decreases progressively from 15.5% (J14) to 4.4% (J14-Li), accompanied by concurrent increases in O_v (54.9% → 58.3%) and O_{ad} (29.6% → 37.3%). This compositional evolution confirms that Li modification concurrently promotes O_v generation and O_{ad} stabilization.

To study the reduction behavior of the catalysts, fresh J14, J14-Li_1Zn_3, and J14-Li catalysts were subjected to H_2-TPR analysis (Fig. S14). For J14, reduction peaks at 187 °C and 204 °C are attributed to stepwise $Cu^{2+} \rightarrow Cu^{+} \rightarrow Cu^{0}$ reduction, while the feature at 253 °C corresponds to Co^{2+}/Ni^{2+} reduction.[49–51] The broad peak at 631 °C is attributed to lattice oxygen reduction accompanied by structural collapse due to over-reduction.[52] In the Li-doped samples, the lattice oxygen reduction peak progressively shifted to lower temperatures (405 °C, 525 °C, and 584 °C for J14-Li_1Zn_3; 444 °C for J14-Li). Quantitative analysis exhibits that the consumption of H_2 during reduction follows the order of J14-Li (5222.5 μmol g_{cat}^{-1}) > J14-Li_1Zn_3 (4520.5 μmol g_{cat}^{-1}) > J14 (3610.3 μmol g_{cat}^{-1}) (Table S4). These findings indicate that Li doping enhances catalyst reducibility, thereby promoting metal exsolution and oxygen vacancy generation. Given that Co and Ni are established active sites for CH_4, the additional exsolved Co and Ni sites are considered a primary factor contributing to increased CH_4 byproduct formation.[53,54]

Structure–activity relationship study

To gain insights into the adsorption and activation of catalysts acting on reactants, we performed CO_2 temperature-pro-

Open Access Article. Published on 02 Fuulbana 2025. Downloaded on 04/12/2025 4:41:09 AM.
This article is licensed under a Creative Commons Attribution-NonCommercial 3.0 Unported Licence.

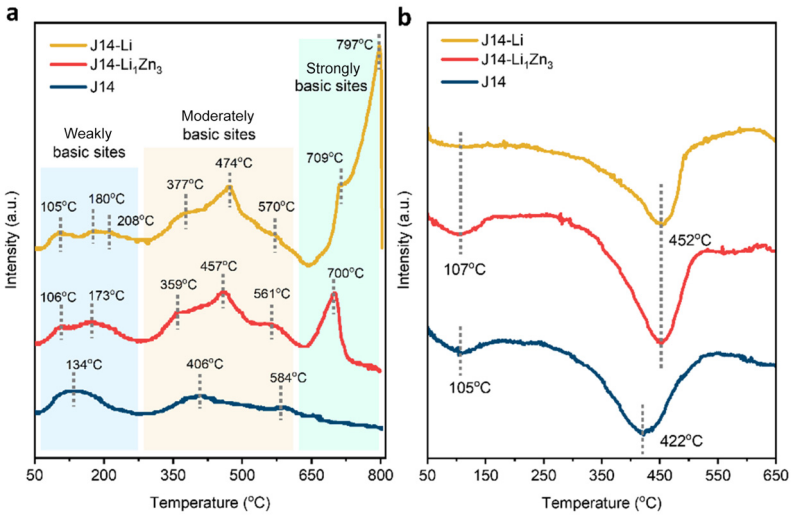

Fig. 6 Chemisorption experiment of used catalysts. (a) CO_2-TPD and (b) H_2-TPD plots of used J14-Li, J14-Li_1Zn_3, and J14.

grammed desorption (CO_2-TPD), H_2-TPD, and H–D exchange mass spectrometry (MS) experiments. In the CO_2-TPD analysis of J14, two types of basic sites are identified (Fig. 6a): one is weakly basic sites, with a peak temperature (T_p) of 134 °C, and the other is moderately basic sites, with T_p in the 300–600 °C range.[55] With the introduction of Li, the overall catalyst basicity is enhanced, where the variety of weakly and moderately basic sites increases, accompanied by the generation of new strongly basic sites. Quantitative analysis reveals that the number of weakly basic sites follows the order of J14-Li_1Zn_3 (6.2 μmol g_{cat}^{-1}) > J14 (5.5 μmol g_{cat}^{-1}) > J14-Li (3.6 μmol g_{cat}^{-1}), and that of moderately basic sites follows the order of J14-Li (23.7 μmol g_{cat}^{-1}) > J14-Li_1Zn_3 (22.7 μmol g_{cat}^{-1}) > J14 (10.5 μmol g_{cat}^{-1}) (Table S5). Meanwhile, the strongly basic sites increase sharply with Li doping (7.1 μmol g_{cat}^{-1} in J14-Li_1Zn_3, 70.6 μmol g_{cat}^{-1} in J14-Li). Literature evidence suggests that weakly and moderately basic sites serve as primary active centers for CO_2 hydrogenation, while excessive CO_2 adsorption on strongly basic sites is counterproductive.[56] In this case, the promotion of effective surface basicity by Li doping approaches saturation in the J14-Li_1Zn_3 catalyst. H_2-TPD analysis reveals that there are two desorption peaks at 105 °C and 422 °C for J14, assigned to physisorbed H_2 and strongly chemisorbed/metal-bound hydrogen species, respectively, with quantitative analysis showing values of 5.5 and 10.5 μmol g_{cat}^{-1} (Fig. 6b and Table S6). For J14-Li_1Zn_3, both peaks shifted to higher temperatures (107 °C and 452 °C), with increased desorption quantities (4.8 and 52.8 μmol g_{cat}^{-1}), indicating enhanced H_2 adsorption. In contrast, J14-Li exhibits decreased desorption quantities of the two hydrogen species (2.5 and 41.7 μmol g_{cat}^{-1}) with a similar desorption temperature, indicating a decline in H_2 adsorption sites. As metal sites are generally regarded to adsorb hydrogen species, this variation could be attributed to an increase in accessible metal sites in J14-Li_1Zn_3 and a decrease in J14-Li. This is in agreement with the modulation of metal sites by Li-doping as shown above. Besides, the HD exchange MS analysis results are shown in Fig. 7a. For J14, the HD signal (m/z = 3) intensity progressively increased from 50 °C and reached equilibrium near 88 °C. The Li-modified J14-Li catalyst demonstrated comparable temperature-dependent behavior but with slightly higher HD signal intensities. Notably, J14-Li_1Zn_3 achieved H/D exchange equilibrium already at 50 °C. These findings conclusively establish a hydrogen dissociation efficiency gradient as follows: J14-Li_1Zn_3 > J14-Li > J14.[56]

Furthermore, elucidating the reaction mechanism is critical for understanding catalytic behavior. The RWGS reaction primarily proceeds through two distinct pathways: redox and associative.[57] In the redox pathway, CO_2 undergoes direct catalytic reduction to CO without requiring hydrogen participation. Conversely, the associative pathway involves sequential surface adsorption of CO_2 followed by hydrogenation to CO. We conducted CO_2 dissociation experiments (Fig. 7b) and CO_2 adsorption–reduction experiments (Fig. 7c and d), with the product signals detected using MS, to identify the redox and associative pathways proceeding.[22] Upon the injection of CO_2 alone at 350 °C (Fig. 7b), CO signals emerged for all samples, with intensities following the order of J14 > J14-Li_1Zn_3 > J14-Li. This indicates the existence of redox pathways in the catalysts, which are progressively suppressed by Li doping. After CO_2 adsorption saturation and subsequent H_2 injection at 350 °C, CO (Fig. 7c) and CH_4 (Fig. 7d) signals appeared, indicating that adsorbed CO_2 undergoes both desired hydrogenation to CO and partial overhydrogenation to CH_4. Notably, CO signal intensities followed the order of J14-Li_1Zn_3 > J14-Li > J14 (Fig. 7c), while CH_4 intensities exhibited the reverse trend: J14-Li > J14-Li_1Zn_3 > J14 (Fig. 7d). The results suggest that Li doping enhances the associative pathway while concomitantly promoting overhydrogenation, with the severity of this side reaction exhibiting a positive correlation with Li content. This is consistent with the optimal promotion of RWGS activity by moderate Li doping (J14-Li_1Zn_3), whereas overdoping yields

 This journal is © the Partner Organisations 2025

Open Access Article. Published on 02 Fuulbana 2025. Downloaded on 04/12/2025 4:41:09 AM.
This article is licensed under a Creative Commons Attribution-NonCommercial 3.0 Unported Licence.

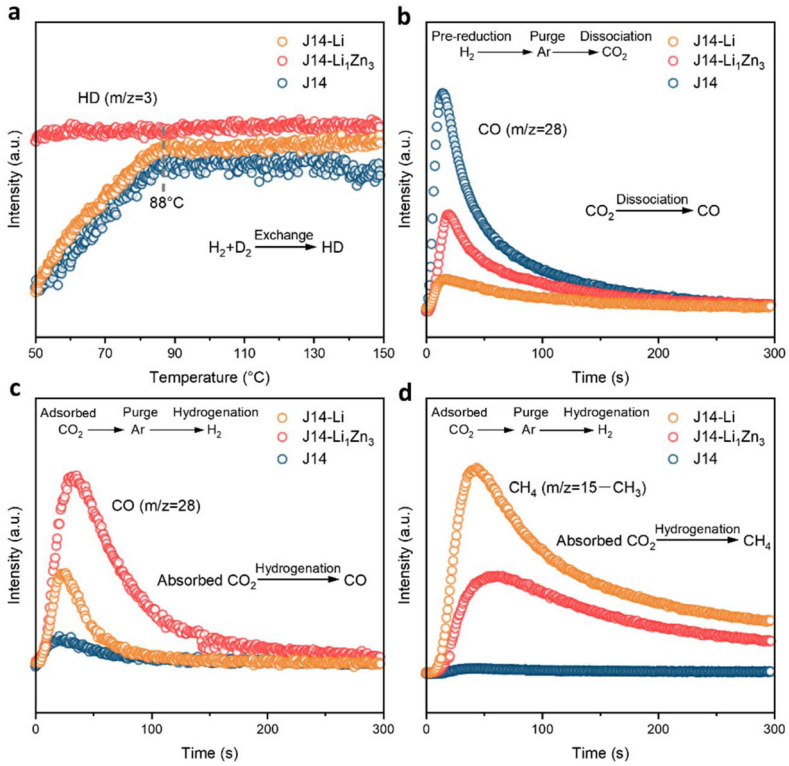

Fig. 7 Chemical reaction mass spectrometry experiments. (a) HD exchange, (b) CO_2 dissociation, and (c and d) CO_2 adsorption–reduction experiments on used J14-Li, J14-Li_1Zn_3, and J14.

severe CH_4 byproducts (J14-Li). Afterward, *in situ* diffuse reflectance infrared Fourier transform spectroscopy (DRIFTS) was performed under sequential inlet of CO_2, N_2 and H_2, to identify the hydrogenation intermediate species in the associative pathway (Fig. S15–S17). Upon CO_2 introduction, carbonate species formed on J14, J14-Li_1Zn_3, and J14-Li surfaces. Switching to N_2 purging induced rapid carbonate desorption from J14, while J14-Li_1Zn_3 exhibited intermediate desorption kinetics and J14-Li retained the most persistent carbonate species. This trend demonstrates that Li incorporation enhances CO_2 adsorption stability, consistent with the CO_2-TPD profiles (Fig. 6a). Subsequent H_2 exposure consumed surface carbonates on J14, generating bicarbonate and formate species. In contrast, carbonate hydrogenation on J14-Li_1Zn_3 and J14-Li predominantly yielded bicarbonate intermediates. These observations suggest that Li doping mainly promotes CO_2 hydrogenation following the carbonate associative pathway.

Conclusions

In conclusion, we demonstrated that substituting Zn with low-valent alkali metal Li^+ in the J14 HEO framework enables dual regulation of metallic sites and surface basicity. Optimal Li loading achieves simultaneous enhancement of RWGS activity and stability, whereas excessive doping triggers gross methanation side reactions. Characterization and structure–activity relationship analyses reveal that moderate Li incorporation improves exsolution and dispersion of Cu, Co, and Ni metals, while elevating the density of weakly and moderately basic sites. This dual effect synergistically facilitates H_2 dissociation and CO_2 activation pathways. Conversely, excessive Li doping induces metallic site aggregation, enriching the methanation-active species Co and Ni, and preferentially generates ineffective strongly basic sites. Additionally, Li doping suppresses the redox pathway while enhancing the associative pathway (carbonate), with CH_4 byproducts originating from over-hydrogenation during the latter. This low-valent alkali metal doping strategy presents a promising approach for enhancing catalytic performance in high-entropy oxide systems.

Author contributions

K. Wang conducted the experiment and, along with R. Zhang and X. Wang, carried out the investigation. K. Wang, X. Wang and J. Xu developed the methodology and wrote the original draft, as well as being involved in the review and editing of the writing. X. Wang, S. Song, J. Xu and H. Zhang conceived and co-supervised the project. All authors participated in the discussion and data analysis.

Conflicts of interest

There are no conflicts to declare.

Open Access Article. Published on 02 Fuulbana 2025. Downloaded on 04/12/2025 4:41:09 AM. This article is licensed under a Creative Commons Attribution-NonCommercial 3.0 Unported Licence.

Data availability

The data supporting this article have been included as part of the SI. Methods, experimental details and supplementary figures. See DOI: https://doi.org/10.1039/d5qi01099c.

Acknowledgements

We thank Y. Zhang for the help in STEM characterization. This work was supported by the financial aid from the National Science and Technology Major Project of China (2021YFB3500700), National Natural Science Foundation of China (22020102003, 22025506, 22271274 and U23A20140), and Jilin Province Science and Technology Development Plan Project (20230101022JC). X. W. acknowledges funding from the National Natural Science Foundation of China Outstanding Youth Science Foundation of China (Overseas).

References

1 Z. Liu, Z. Deng, S. J. Davis and P. Ciais, Global carbon emissions in 2023, *Nat. Rev. Earth Environ.*, 2024, **5**, 253–254.
2 Z. Deng, B. Zhu, S. J. Davis, P. Ciais, D. Guan, P. Gong and Z. Liu, Global carbon emissions and decarbonization in 2024, *Nat. Rev. Earth Environ.*, 2025, **6**, 231–233.
3 Y. Wang, J. Sun and N. Tsubaki, Clever nanomaterials fabrication techniques encounter sustainable C1 catalysis, *Acc. Chem. Res.*, 2023, **56**, 2341–2353.
4 J. Zhong, X. Yang, Z. Wu, B. Liang, Y. Huang and T. Zhang, State of the art and perspectives in heterogeneous catalysis of CO_2 hydrogenation to methanol, *Chem. Soc. Rev.*, 2020, **49**, 1385–1413.
5 X. Zhang, W. Huang, L. Yu, M. García-Melchor, D. Wang, L. Zhi and H. Zhang, Enabling heterogeneous catalysis to achieve carbon neutrality: Directional catalytic conversion of CO_2 into carboxylic acids, *Carbon Energy*, 2024, **6**, e362.
6 S. Liu, Q. Zhao, X. Han, C. Wei, H. Liang, Y. Wang, S. Huang and X. Ma, Proximity effect of Fe–Zn Bimetallic catalysts on CO_2 hydrogenation performance, *Trans. Tianjin Univ.*, 2023, **29**, 293–303.
7 A. N. Matveyeva and S. O. Omarov, Comparison of perovskite systems based on $AFeO_3$ (A = Ce, La, Y) in CO_2 hydrogenation to CO, *Trans. Tianjin Univ.*, 2024, **30**, 337–358.
8 Y. Wang, Y. Liu, L. Tan, X. Lin, Y. Fang, X. F. Lu, Y. Hou, G. Zhang and S. Wang, Confining ultrafine Pt nanoparticles on In_2O_3 nanotubes for enhanced selective methanol production by CO_2 hydrogenation, *J. Mater. Chem. A*, 2023, **11**, 26804–26811.
9 X. Yue, X. Liu, K. Wang, Z. Yang, X. Chen, W. Dai and X. Fu, Photo-assisted thermal catalytic Fischer–Tropsch synthesis over Co–Cu/CeO_2, *Inorg. Chem. Front.*, 2022, **9**, 1258–1269.
10 M. Irshad, H. Jo, S. Ahmed, W. Yoon, S. K. Kim, H. J. Chun and J. Kim, Tandem reductive hydroformylation: A mechanism for selective synthesis of straight-chain α-alcohols by CO_2 hydrogenation, *Appl. Catal., B*, 2025, **365**, 124978.
11 A. M. Bahmanpour, M. Signorile and O. Kröcher, Recent progress in syngas production via catalytic CO_2 hydrogenation reaction, *Appl. Catal., B*, 2021, **295**, 120319.
12 Q. Wang, X. Liu, D. He and D. Wang, Fundamental comprehension, synthetic procedures and catalytic applications of high entropy oxide nanomaterials, *Mater. Today*, 2023, **70**, 218–236.
13 J. Zou, L. Tang, W. He and X. Zhang, High-entropy oxides: Pioneering the future of multifunctional materials, *ACS Nano*, 2024, **18**, 34492–34530.
14 X. Liu, S. Huang, D. Yuan, S. Li, L. Ma, L. Gao, Z. Li, Y. Wang, Y. Li and J. Ye, High-entropy-assisted platinum single atoms for photothermal green syngas production with high CO_2 utilization efficiency, *Inorg. Chem. Front.*, 2025, **12**, 4041–4047.
15 S. Hanabata, K. Kusada, T. Yamamoto, T. Toriyama, S. Matsumura, S. Kawaguchi, Y. Kubota, Y. Nishida, M. Haneda and H. Kitagawa, Denary high-entropy oxide nanoparticles synthesized by a continuous supercritical hydrothermal flow process, *J. Am. Chem. Soc.*, 2024, **146**, 181–186.
16 J. Mi, X. Chen, Y. Ding, L. Zhang, J. Ma, H. Kang, X. Wu, Y. Liu, J. Chen and Z.-S. Wu, Activation of partial metal sites in high-entropy oxides for enhancing thermal and electrochemical catalysis, *Chin. J. Catal.*, 2023, **48**, 235–246.
17 K. Wang, R. Zhang, H. Wang, L. Zhang, Z. Wang, X. Wang, S. Song and H. Zhang, Rh-loaded high-entropy oxide for efficiently catalyzing the reverse water-gas shift reaction, *Chem. Res. Chin. Univ.*, 2024, **40**, 970–977.
18 M. Cortazar, M. Lafuente, A. Navarro-Puyuelo, X. Garcia, J. Llorca, I. Reyero, F. Bimbela and L. M. Gandía, Highly selective CO formation via CO_2 hydrogenation over novel ceria-based high-entropy oxides (HEOs), *Chem. Eng. J.*, 2025, **507**, 160706.
19 S. Hou, X. Ma, Y. Shu, J. Bao, Q. Zhang, M. Chen, P. Zhang and S. Dai, Self-regeneration of supported transition metals by a high entropy-driven principle, *Nat. Commun.*, 2021, **12**, 5917.
20 J. Zhao, J. Bao, S. Yang, Q. Niu, R. Xie, Q. Zhang, M. Chen, P. Zhang and S. Dai, Exsolution–dissolution of supported metals on high-entropy $Co_3MnNiCuZnO_x$: Toward sintering-resistant catalysis, *ACS Catal.*, 2021, **11**, 12247–12257.
21 H. X. Liu, J. Y. Li, X. Qin, C. Ma, W.-W. Wang, K. Xu, H. Yan, D. Xiao, C. J. Jia, Q. Fu and D. Ma, Pt_n–O_v synergistic sites on MoO_x/γ-Mo_2N heterostructure for low-temperature reverse water–gas shift reaction, *Nat. Commun.*, 2022, **13**, 5800.
22 H. X. Liu, S. Q. Li, W.-W. Wang, W. Z. Yu, W.-J. Zhang, C. Ma and C.-J. Jia, Partially sintered copper-ceria as excellent catalyst for the high-temperature reverse water gas shift reaction, *Nat. Commun.*, 2022, **13**, 867.
23 X. Zhang, X. Zhu, L. Lin, S. Yao, M. Zhang, X. Liu, X. Wang, Y.-W. Li, C. Shi and D. Ma, Highly dispersed copper over β-Mo_2C as an efficient and stable catalyst for the reverse

 This journal is © the Partner Organisations 2025

Open Access Article. Published on 02 Fuulbana 2025. Downloaded on 04/12/2025 4:41:09 AM.
This article is licensed under a Creative Commons Attribution-NonCommercial 3.0 Unported Licence.

water gas shift (RWGS) reaction, *ACS Catal.*, 2017, **7**, 912–918.

24 H. Wang, M. S. Bootharaju, J. H. Kim, Y. Wang, K. Wang, M. Zhao, R. Zhang, J. Xu, T. Hyeon, X. Wang, S. Song and H. Zhang, Synergistic interactions of neighboring platinum and iron atoms enhance reverse water–gas shift reaction performance, *J. Am. Chem. Soc.*, 2023, **145**, 2264–2270.

25 R. Zhang, X. Wang, K. Wang, H. Wang, L. Liu, X. Wu, B. Geng, X. Chu, S. Song and H. Zhang, Synergism of ultrasmall pt clusters and basic $La_2O_2CO_3$ supports boosts the reverse water gas reaction efficiency, *Adv. Energy Mater.*, 2023, **13**, 2203806.

26 Y. Zhou, A. Sadia Traore, D. V. Peron, A. J. Barrios, S. A. Chernyak, M. Corda, O. V. Safonova, A. Iulian Dugulan, O. Ersen, M. Virginie, V. V. Ordomsky and A. Y. Khodakov, Promotion effects of alkali metals on iron molybdate catalysts for CO_2 catalytic hydrogenation, *J. Energy Chem.*, 2023, **85**, 291–300.

27 Q. Yang, V. A. Kondratenko, S. A. Petrov, D. E. Doronkin, E. Saraçi, H. Lund, A. Arinchtein, R. Kraehnert, A. S. Skrypnik, A. A. Matvienko and E. V. Kondratenko, Identifying performance descriptors in CO_2 hydrogenation over iron-based catalysts promoted with alkali metals, *Angew. Chem., Int. Ed.*, 2022, **61**, e202116517.

28 X. Wang, E. Toshcheva, A. Rendón-Patiño, C. Martín, U. H. Bhatti, D. Mateo, R. Ahmad, M. H. Alabsi, L. Cavallo, J. M. R. Gallo and J. Gascon, Indium oxide modified with alkali metals: A selective catalyst for the reverse water-gas shift reaction at high pressure, *Chem. Eng. J.*, 2025, **507**, 160326.

29 N. Zhang, A. Naden, L. Zhang, X. Yang, P. Connor and J. Irvine, Enhanced CO_2 electrolysis through Mn substitution coupled with Ni exsolution in lanthanum calcium titanate electrodes, *Adv. Mater.*, 2024, **36**, 2308481.

30 W. Lin, W. Su, Y. Li, T.-W. Chiu, M. Singh, Z. Pan and L. Fan, Enhancing electrochemical CO_2 reduction on perovskite oxide for solid oxide electrolysis cells through in situ A-site deficiencies and surface carbonate deposition induced by lithium cation doping and exsolution, *Small*, 2023, **19**, 2303305.

31 O. Kwon, S. Sengodan, K. Kim, G. Kim, H. Y. Jeong, J. Shin, Y.-W. Ju, J. W. Han and G. Kim, Exsolution trends and co-segregation aspects of self-grown catalyst nanoparticles in perovskites, *Nat. Commun.*, 2017, **8**, 15967.

32 K. Park, M. Saqib, H. Lee, D. Shin, M. Jo, K. M. Park, M. Hamayun, S. H. Kim, S. Kim, K.-S. Lee, R. O'Hayre, M. Choi, S.-J. Song and J.-Y. Park, Water-mediated exsolution of nanoparticles in alkali metal-doped perovskite structured triple-conducting oxygen electrocatalysts for reversible cells, *Energy Environ. Sci.*, 2024, **17**, 1175–1188.

33 H. Chen, C. Lim, M. Zhou, Z. He, X. Sun, X. Li, Y. Ye, T. Tan, H. Zhang, C. Yang, J. W. Han and Y. Chen, Activating lattice oxygen in perovskite oxide by B-site cation doping for modulated stability and activity at elevated temperatures, *Adv. Sci.*, 2021, **8**, 2102713.

34 Z. Luo, X. Ge, D. Fang, X. Xu, D. Zhang, Y. Cao, X. Duan, W. Li, J. Zhou and X. Zhou, In situ exsolution to fabricate interfacial $Ni^0/Ni^{\delta+}$ sites for regulating reaction pathways in hydrogenation, *J. Catal.*, 2024, **434**, 115528.

35 H. Kang, L. Zhu, S. Li, S. Yu, Y. Niu, B. Zhang, W. Chu, X. Liu, S. Perathoner, G. Centi and Y. Liu, Generation of oxide surface patches promoting H-spillover in Ru/(TiO_x) MnO catalysts enables CO_2 reduction to CO, *Nat. Catal.*, 2023, **6**, 1062–1072.

36 X. Song, Y. Jiang, X. Dang and Z. Gao, In situ exsolved mangosteen-type nanoalloy clusters and engineered heterogeneous interfaces for high-performance fuel-flexible solid oxide cells, *Small*, 2025, **21**, 2412437.

37 Q. Sun, X. Hao, T. Zhang, Z. Ma, K. Hu, M. Yang, X. Huang and X. Liu, An electrodeposited superaerophobic nickel catalyst on pencil-drawn paper: a novel approach for highly efficient and stable hydrogen evolution, *Inorg. Chem. Front.*, 2024, **11**, 3348–3356.

38 Y. Zheng, H. Chen, Z. Zhou, Y. Yang, M. Zou, W. Zhang, B. Wei, J. Cai, J.-L. Lan, D. Yi, C.-W. Nan and Y.-H. Lin, Electrical property enhancement in orientation-modulated perovskite La-doped $SrTiO_3$ thermoelectric thin films, *Adv. Funct. Mater.*, 2023, **33**, 2301815.

39 T. Li, Y. Yao, Z. Huang, P. Xie, Z. Liu, M. Yang, J. Gao, K. Zeng, A. H. Brozena, G. Pastel, M. Jiao, Q. Dong, J. Dai, S. Li, H. Zong, M. Chi, J. Luo, Y. Mo, G. Wang, C. Wang, R. Shahbazian-Yassar and L. Hu, Denary oxide nanoparticles as highly stable catalysts for methane combustion, *Nat. Catal.*, 2021, **4**, 62–70.

40 A. Roy, S. Hettler and R. Arenal, Direct visualization of temperature-induced phase separation of completely miscible Au–Pd alloy by in situ TEM, *Small*, 2025, **21**, 2408109.

41 H. Yang, X. Mu, J. Guan, B. Ouyang, H. Li and Y. Deng, Steady Cu^+ species via magnesium and boron co-modification for enhanced CO_2 electroreduction to C_{2+} products: an in situ Raman spectroscopic study, *Inorg. Chem. Front.*, 2024, **11**, 4770–4779.

42 Z. Liu, X. Gao, B. Liu, W. Song, Q. Ma, T.-s. Zhao, X. Wang, J. W. Bae, X. Zhang and J. Zhang, Highly stable and selective layered Co-Al-O catalysts for low-temperature CO_2 methanation, *Appl. Catal., B*, 2022, **310**, 121303.

43 L. Li, L. Wang, X. Peng, S. Tao and M.-H. Zeng, Nickel–salen as a model for bifunctional OER/UOR electrocatalysts: pyrolysis temperature–electrochemical activity interconnection, *Inorg. Chem. Front.*, 2022, **9**, 1973–1983.

44 A. Naderi, M. Jourshabani and B.-K. Lee, Effects of d-block transition metal impurities on a carbon Cloth/$Ni(OH)_2$ interface for electrocatalytic oxygen evolution reaction, *ACS Sustainable Chem. Eng.*, 2023, **11**, 9010–9019.

45 M. R. A. Cruz, E. Luévano-Hipólito, R. Garza-Hernández and L. M. Torres-Martínez, MgO and $Mg(OH)_2$ thin films prepared by the SILAR method and their CO_2 photocatalytic performance, *J. Mater. Sci.*, 2022, **57**, 18739–18753.

46 H. Li, B. Yu and H. Yu, An efficient and stable inverted structure organic solar cell using ZnO modified by 2D $ZrSe_2$ as a composite electron transport layer, *Adv. Funct. Mater.*, 2024, **34**, 2402128.

Open Access Article. Published on 02 Fuulbana 2025. Downloaded on 04/12/2025 4:41:09 AM.
This article is licensed under a Creative Commons Attribution-NonCommercial 3.0 Unported Licence.

47 K. N. Wood and G. Teeter, XPS on Li-battery-related compounds: Analysis of inorganic SEI phases and a methodology for charge correction, *ACS Appl. Energy Mater.*, 2018, **1**, 4493–4504.

48 B. Xiao, X. Liu, Z. Xie, D. Zheng, J. Zha, J. Qi, F. Wei, Q. Meng, X. Xue, D. Zhao, Y. Li, Q. Yin, L. Ma, M. Ge, X. Xiao, Y. Sui, S. Chen and J. Zheng, Zero-strain high entropy spinel oxide $(FeNiCuCrMn)_3O_4$@rGO as high-performance anode for sodium ion battery, *Chem. Eng. J.*, 2025, **503**, 158269.

49 S. Li, X. Liu, J. Ma, F. Xu, Y. Lyu, S. Perathoner, G. Centi and Y. Liu, Develop high-performance Cu-based RWGS catalysts by controlling oxide–oxide interface, *ACS Catal.*, 2025, **15**, 3475–3486.

50 S. Mo, Q. Zhang, Y. Sun, M. Zhang, J. Li, Q. Ren, M. Fu, J. Wu, L. Chen and D. Ye, Gaseous CO and toluene co-oxidation over monolithic core–shell Co_3O_4-based heterostructured catalysts, *J. Mater. Chem. A*, 2019, **7**, 16197–16210.

51 F. Jing, S. Liu, R. Wang, X. Li, Z. Yan, S. Luo and W. Chu, Hydrogen production through glycerol steam reforming over the $NiCe_xAl$ catalysts, *Renewable Energy*, 2020, **158**, 192–201.

52 E. Gao, Q. Jin, T. Zhang, L. Han, N. Li, J. Xu, S. Yao, Z. Wu, J. Li, J. Zhu and W. Wang, Unraveling the promotional effects of K-doping on the mobility of surface oxygen species of $CoCr_2O_4$ for improved formaldehyde catalytic oxidation: The weakened metal-oxygen bond strength, *Chem. Eng. J.*, 2023, **474**, 145618.

53 H. Zhang, D. Cui, T. Shen, T. He, D. Sun, S. An, B. Qi and Y.-F. Song, Engineering of PMo12@NiCo-LDH composite via in situ encapsulation-reassembly strategy for highly selective photocatalytic reduction of CO_2 to CH_4, *Inorg. Chem. Front.*, 2023, **10**, 1421–1430.

54 W. Wang, M. Nguyen-Quang, D. Mateo, X. Yong, T. Li, H. Xie, W. Chu, C. Pham-Huu, X. Tu and J. Gascon, A review of CO_2 methanation process: Recent advances and future prospects, *ACS Catal.*, 2025, **15**, 10868–10896.

55 M. Gu, S. Dai, R. Qiu, M. E. Ford, C. Cao, I. E. Wachs and M. Zhu, Structure–activity relationships of copper- and potassium-modified iron oxide catalysts during reverse water–gas shift reaction, *ACS Catal.*, 2021, **11**, 12609–12619.

56 X. Liang, X. Jin, S. Yu, C. Li, C. Song, G. Sheng, X. Ye, R. Gao, L. Lin and D. Ma, CO-resistant hydrogenation over noble metal/α-MoC catalyst, *Nat. Commun.*, 2025, **16**, 4159.

57 M. L. T. Triviño, N. C. Arriola, Y. S. Kang and J. G. Seo, Transforming CO_2 to valuable feedstocks: Emerging catalytic and technological advances for the reverse water gas shift reaction, *Chem. Eng. J.*, 2024, **487**, 150369.

This journal is © the Partner Organisations 2025